DOI 10.1515/bmt-2012-0044 — Biomed Tech 2013; 58(4): 359–367

Research article

Sabine Donner*, Oliver Müller, Frank Witte, Ivonne Bartsch[a], Elmar Willbold, Tammo Ripken, Alexander Heisterkamp[b], Bodo Rosenhahn and Alexander Krüger

In situ optical coherence tomography of percutaneous implant-tissue interfaces in a murine model

Abstract: Novel surface coatings of percutaneous implants need to be tested in biocompatibility studies. The use of animal models for testing usually involves numerous lethal biopsies for the analysis of the implant-tissue interface. In this study, optical coherence tomography (OCT) was used to monitor the reaction of the skin to a percutaneous implant in an animal model of hairless but immunocompetent mice. *In vivo* optical biopsies with OCT were taken at days 7 and 21 after implantation and *post mortem* on the day of noticeable inflammation. A Fourier-domain OCT was programmed for spoke pattern scanning schemes centered at the implant midpoint to reduce motion artifacts during *in vivo* imaging. Image segmentation allowed the automatic detection and morphometric analysis of the skin contour and the subcutaneous implant anchor. On the basis of the segmentation, the overall refractive index of the tissue within one OCT data set was estimated as a free parameter of a fitting algorithm, which corrects for the curved distortion of the planar implant base in the OCT images. OCT in combination with the spoke scanning scheme and image processing provided time-resolved three-dimensional optical biopsies around the implants to assess tissue morphology.

Keywords: *in vivo*; motion artifacts; refractive index; scanning scheme; segmentation.

[a]Currently affiliated with the Department of Experimental Otology, Institute of Audioneurotechnology, Hannover Medical School, D-30625 Hannover, Germany.
[b]To the time point of the study, affiliated with Biomedical Optics Department, Laser Zentrum Hannover e.V., D-30419 Hannover, Germany and also with CrossBIT, Hannover Medical School, 30625 Hannover, Germany.
***Corresponding author: Sabine Donner,** Biomedical Optics Department, Laser Zentrum Hannover e.V., D-30419 Hannover, Germany, Phone: +49 511 2788 325, Fax: +49 511 2788 100, E-mail: s.donner@lzh.de

Sabine Donner and Alexander Krüger: CrossBIT, Hannover Medical School, 30625 Hannover, Germany
Oliver Müller and Bodo Rosenhahn: Institute for Information Processing, Leibniz University of Hannover, D-30167 Hannover, Germany
Frank Witte, Ivonne Bartsch and Elmar Willbold: Department of Orthopaedics/CrossBIT, Hannover Medical School, 30625 Hannover, Germany
Tammo Ripken and Alexander Krüger: Biomedical Optics Department, Laser Zentrum Hannover e.V., D-30419 Hannover, Germany
Alexander Heisterkamp: Institute of Applied Optics, Friedrich-Schiller-University Jena, D-07743 Jena, Germany

Introduction

Percutaneous implants are used for the osseointegrated fixation of exoprostheses to provide more physiological load transmission onto the skeleton of the patient than conventional stump-socket interfaces do [21]. The implant-tissue interface where the prosthesis penetrates the skin is prone to inflammation, which can lead to implant failure [24]. To avoid inflammation, different implant designs and coatings were developed and tested in biocompatibility studies in animal models [19, 20, 24]. Morphological features such as epithelial downgrowth and the inflammatory response were analyzed in histological images obtained from tissue sections [6]. One drawback of the study protocol is the high animal consumption for the time-dependent monitoring of foreign body reaction. Another limitation arises from the embedding and preparation artifacts during histological procedures, which limits the number of sections available for quantitative analysis [6]. Using non-contact *in vivo* imaging for postoperative monitoring of the implant-tissue interface would lead to a more efficient study protocol with reduced animal numbers. Optical coherence tomography (OCT) was developed as a non-invasive imaging technique to provide optical biopsies of tissue [8]. Fourier-domain

OCT (FD-OCT) is based on low-coherence spectral interferometry [3] and was shown to be an effective tool for imaging the skin [4, 5] and for the measurement of thicknesses of the primary layers of the skin [14, 26].

In this study, FD-OCT was used in parallel to a conventional biocompatibility study, testing percutaneous devices in a hairless mice animal model to gain information about tissue morphology, which is complementary to the endpoint biopsies. OCT enables the non-invasive monitoring of the implant-tissue interface at various time points in the same animal at arbitrary positions on the circular implant. With the *in vivo* setting of the experiment, the challenge of motion artifacts in the OCT images arises due to breathing and pulse of the animals. Depending on the sample and motion characteristic, different concepts for motion compensation either during image acquisition or by means of image postprocessing have been published for OCT applications. Methods used during image acquisition include increasing the imaging speed to reduce acquisition time [11], triggering acquisition by synchronization of OCT data with an independent measurement of the phase of the respiratory cycle [15], and adapting the scanning scheme to the individual application [16]. In accordance with recent publications [13], we observed that the effect of motion artifacts is significantly smaller in single brightness scans (B-scans) (fast scanning axis) than in subsequent B-scans forming classic three-dimensional (3D) stacks. Therefore, we applied a spoke scan pattern especially suited for the circular geometry of the implant, in addition to 3D dense scans for each sample. Artifact reduction by image postprocessing concentrates on intensity-based image registration [9] or feature-based image registration [13]. In intensity-based registration methods, the challenge of distinguishing between sample movement and real surface structure arises. By applying the dense and spoke pattern scanning schemes to the same sample, each lateral point was scanned at different time points. Thus, shifts are due to sample motion as the sample structure stays the same. This assumption was used in our previously published algorithm [17] to correct spoke pattern images for motion within the acquisition time of single B-scans.

A subsequent problem addressed in this study is the estimation of the refractive index of the tissue by ray tracing the OCT beam to the original source of scattering. In principle, the refractive index can be computed if the geometrical thickness is known, as demonstrated by Tearney et al. [22]. In their study, the refractive index of excised human dermis was determined by placing the tissue on a planar reference plane and analyzing the OCT image. The same approach was used by Uhlhorn et al. [23] to estimate the refractive index of isolated crystalline lenses and was extended by correction for ray refraction on the sample surface by Westphal et al. [27] and Kim et al. [10]. In our study, the flatness of the base of the implant served as a figure of merit in estimating the refractive index without *a priori* knowledge of the geometrical axial position. The overall refractive index was used to measure the geometrical tissue thickness in OCT images and was also investigated as a potential indicator of inflammation.

Materials and methods

Animal model

The animal experiment was conducted in accordance with German federal animal welfare legislation (Ref.-No. 33.9-42502-04-08/1498) and the National Institute of Health guidelines for the use of laboratory animals.

Immunocompetent hairless mice (type Crl:SKH1-*hr*; Charles River Laboratories, Sulzfeld, Germany) were used to study the biocompatibility of percutaneous implants and to monitor the possible inflammatory response of the skin. The percutaneous implants that were used in this study consisted of a round anchor and a 3-mm-thick and 5-mm-long pin in the middle (see schematic in Figure 1). These were inserted into a percutaneous location caudal to the left costal arch of the mice. The base implanted under the skin contained eight holes allowing the tissue to grow in. The pin was located transcutaneously.

During implantation and OCT measurements, the mice were anesthetized by intraperitoneal injection of 2% xylazine (10 mg/kg body weight; Rompun; Bayer Health Care, Leverkusen, Germany) and 10% ketamine (100 mg/kg body weight; KetaminGraeub; Albrecht GmbH, Aulendorf, Germany). To avoid hypothermia in the mice, the animals were fixed on a custom-made animal-positioning table

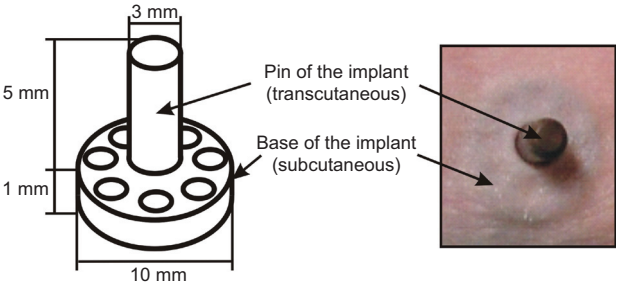

Figure 1 Schematic of the percutaneous implant (left) and a photograph of the implanted pin (right).
The implant consists of a transcutaneous pin and a subcutaneous base.

equipped with a heating pad. The table also restricted the movement of the mice and could be tilted to align the implant in the optical path of the sample beam. *In vivo* OCT scans were taken at days 7 and 21 after implantation. After visible signs of inflammation, e.g., redness or swelling of the skin, next to the implant, mice were sacrificed and *post mortem* OCT scans were taken. The implants with the surrounding skin were then explanted.

OCT setup

The optical setup of the custom-developed FD-OCT system is shown in Figure 2. A superluminescent diode (SLD) (SLD-371-HP1; Superlum, Carrigtwohill, Ireland) emitting light with a central wavelength of λ_0=841.3 nm and a spectral bandwidth of $\Delta\lambda$=47.7 nm (full width at half maximum) was used and defined the theoretical axial resolution of the system to be 6.6 µm (assuming a Gaussian light source spectrum). The light is coupled into an optical fiber and guided to the scanning head where it passes through an interferometer. Two galvanometer-mounted mirrors (6210H; Cambridge Technology, Lexington, MA, USA) scan the sample beam with an A-line-rate of 8 kHz. The objective has a focal length of 25 mm and determines the lateral resolution of 8.7 µm. The light reflected by the scattering structures of the sample and the reference light are merged and coupled into the fiber. A fiber circulator directs the light to a spectrometer while isolating the SLD against back reflections. In the spectrometer, the light is dispersed by a diffractive grating (NT55-262; Edmund Optics GmbH, Karlsruhe, Germany) and focused onto a 2048 pixel (px) charge coupled device (CCD) line camera (runner ruL2048-30gm; Basler AG, Ahrensburg, Germany). The scanning head is equipped with an additional complementary metal-oxide semiconductor camera (Firefly MV; Point Grey Research Inc., Richmond, BC, Canada) for monitoring of the positioning of the sample, for the acquisition of top-view images and to select the region of interest (ROI) before the start of the OCT scan.

Image acquisition modes

The OCT system was programmed for three different scan patterns: (I) preview cross scans; (II) a 72-spoke pattern, centered at the midpoint of the pin; and (III) a dense volume scan.

Video images and mode (I) perpendicular B-scans, crossing each other in the middle of the ROI, were displayed continuously for sample alignment. By moving the OCT scanning head, the midpoint of the ROI was centered at the midpoint of the circular implants. The symmetry axis of the implant was aligned to be parallel to the optical axis to avoid shadowing by the percutaneous pin and to minimize the skew of the implant base.

For subsequent OCT data recording, an ROI of 6 mm × 6 mm with a lateral distance of the amplitude scans (A-scans) of 7.5 µm/px and 4.7 µm/px axial sampling in air was chosen. Data sets were recorded by mode (II) spoke pattern and mode (III) 3D stacks for each sample. Additionally, top-view camera images were saved for documentation of sample alignment and ROI.

Motion compensation

Axial sample motion within the acquisition time of one B-scan needs to be corrected before image undistortion for *in vivo* OCT images. To distinguish sample shape from movement, data from 3D stacks and spoke pattern were combined, creating multiple A-sans of the same position at different time points. Their axial displacement was interpreted to be sample motion due to the shape staying the same. Motion correction was based on the assumption of the similarity of adjacent A-scans within one B-scan

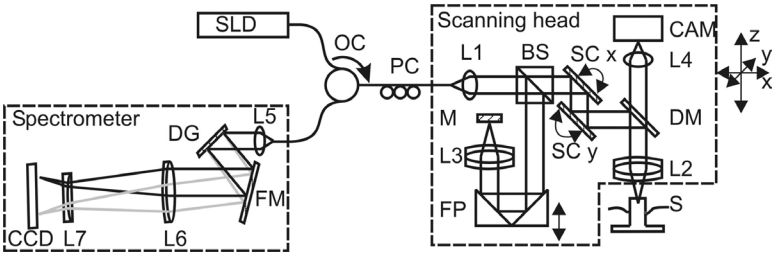

Figure 2 Optical setup of the FD-OCT system.
SLD, superluminescent diode; OC, optical circulator; PC, polarization controller; L1–L7, lenses; BS, beam splitter; SC, scanning mirrors; DM, dichroic mirror; S, sample; CAM, video camera; FP, silver-coated folding mirrors; M, silver mirror; DG, diffractive grating; FM, folding mirror; CCD, line scan camera.

and correlating A-scans taken at the same position at different time points, as described in detail by Müller et al. [17].

Image undistortion

OCT B-scans are formed by A-scans, representing the reflectivity profile at a certain lateral position of the sample. All axial distances are in optical path lengths and therefore need to be corrected by the refractive index to gain images with geometrical dimensions. Additional image deformation is caused by refraction of rays traveling through material. The strongest refraction occurs when the beam penetrates the surface of the sample as there is the highest refractive index step. Because of these effects, the base plate of the implant occurs as a deformed line in the B-scans due to refraction of the beam by the tissue above the metal plate. This is used to gain information about the refractive index of the tissue and simultaneously correct the images for geometrical distances.

As the mouse skin is an uneven surface, a 3D approach needs to be applied. Regardless of the layered structure of the skin, a constant refractive index within the tissue is assumed. Even though the geometrical depth of the implant base is unknown for a single A-scan, the flat shape of the plate allows the assumption that the base reflection forms an even plane in the whole 3D data set. Customized image processing routines were established to correct the images and estimate an overall refractive index of the tissue.

First, owing to the absence of useful image information, the area where the implant pin is located is excluded from the volume image. To this end, the pin boundaries are detected by calculating the first partial derivative of the gray value image intensities along the x-axis for each B-scan using a Sobel filter. The absolute values are summed over each A-scan, which leads to a 2D accumulated image, wherein the pin boundary is obtained by ellipse fitting using the method of Xie [28] with slight modifications, which are described in more detail by Müller et al. [18].

In the next image processing step, the skin surface needs to be segmented. Markov random fields [12] were used. The skin is modeled as a smooth membrane $f(X, Y)=Z$, having no discontinuities except for the hole at the pin position. See Müller et al. [18] for a detailed description.

After segmentation of the skin surface, a surface normal at each lateral position is derived to apply Snell's law of refraction. Before the approximation of the surface normal, the skin is smoothed by using the Loess regression [2]. To this end, for each skin sample point, a surface regression with a second-order polynomial is applied by considering its local neighbourhood with fixed radius. The neighborhood span is chosen to be 1/10 of the X-/Y-axis range. The surface normals are then calculated using the first partial derivatives of the regression polynomials at its origin. The computed normals are shown as blue line segments in Figure 3A. In the next step, each A-scan is tilted below the skin surface for a set of possible refractive indices. For correct ray tracing, the refractive index n' has

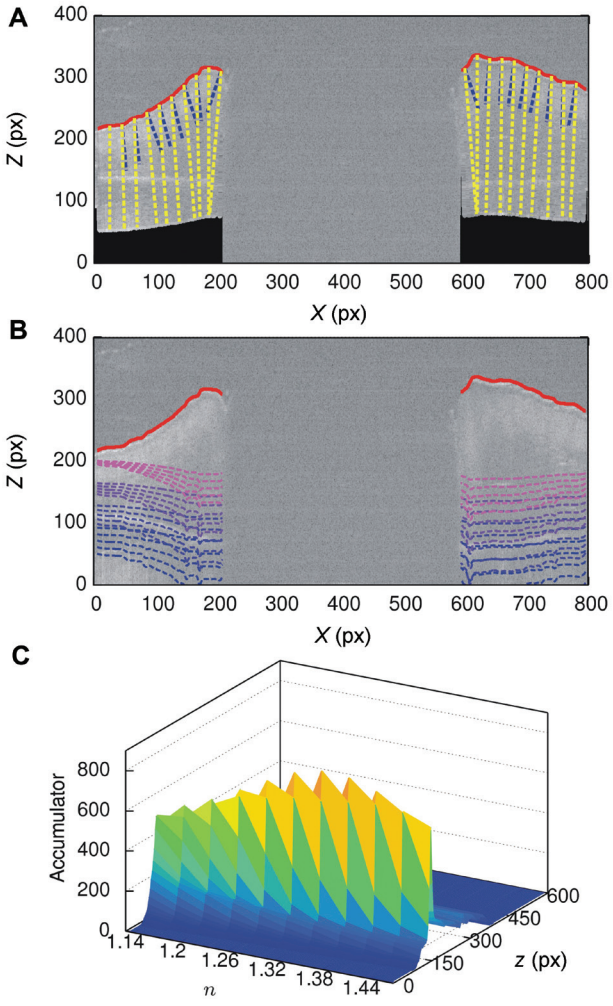

Figure 3 (A) B-scan with segmented skin surface (red contour), approximated surface normals (blue), and resulting ray refraction (yellow) for a given refractive index n. (B) B-scan with segmented skin contour (red) and examples of deformed contours for possible configurations of the parameters n', z, θ_x, and θ_y, where pink lines are examples for low z and blue for high z values. The highest agreement of deformed contour and implant-baseline reflex is computed by parameter estimation using a generalized Hough transform. (C) A subspace of the Hough transform accumulator array for the variables n', z, whereas θ_x and θ_y were kept constant.

to be known. To model the base contour, some additional parameters such as the geometrical depth of the implant base z and tilt angles of the implant base θ_x and θ_y have to be estimated. A cost problem in four dimensions, which represents the four parameters z', n', θ_x and θ_y, is solved by a generalized Hough transform approach [1], as shown in Figure 3C. The parameters are first discretized to span a four-dimensional accumulator array $T(z, n', \theta_x, \theta_y)$. Each accumulator array entry $T(z^{(i)}, n'^{(i)}, \theta_x^{(i)}, \theta_y^{(i)})$ represents one possible contour $c^{(i)}$ [parameterized by $(z^{(i)}, n'^{(i)}, \theta_x^{(i)}, \theta_y^{(i)})$ of the implant base in the OCT volume data set]. The value of this entry represents the support of the contour in the OCT volume. The higher the value, the more likely the parameters corresponding to the array entry describe the true implant base contour. As the implant base contour is characterized by an edge in the OCT scans along the lateral direction, a Sobel edge filter is used, giving high absolute pixel intensities at edges along lateral directions such as the baseline contour and low pixel intensities otherwise. For each array entry $T(z^{(i)}, n'^{(i)}, \theta_x^{(i)}, \theta_y^{(i)})$, its value is computed by incrementing and accumulating its entry value for each edge pixel intersecting the contour $c^{(i)}$ with parameters $(z^{(i)}, n'^{(i)}, \theta_x^{(i)}, \theta_y^{(i)})$ of a certain amount, which is usually set to 1. In our approach, we increment the value by the absolute edge pixel intensity for better discrimination of weak and noisy edges.

The geometrical depth z is sampled in one pixel step size, $n' \in [1.3 \ldots 1.5]$ in 0.01 steps and $\theta_x^{(i)}, \theta_y^{(i)} \in [-5 \ldots 5]$ in half-degree steps. For each possible hypothetical refractive index, undistortion of the image is performed as shown in Figure 3B for some examples, n', θ_x, θ_y, represented by the pink, purple and blue line sets. The maximum in the accumulator array T (see Figure 3C, showing a subspace in n', z whereby the other parameters are constant) yields the optimal parameters $(z, n', \theta_x, \theta_y)$ from which the geometrically corrected image is computed.

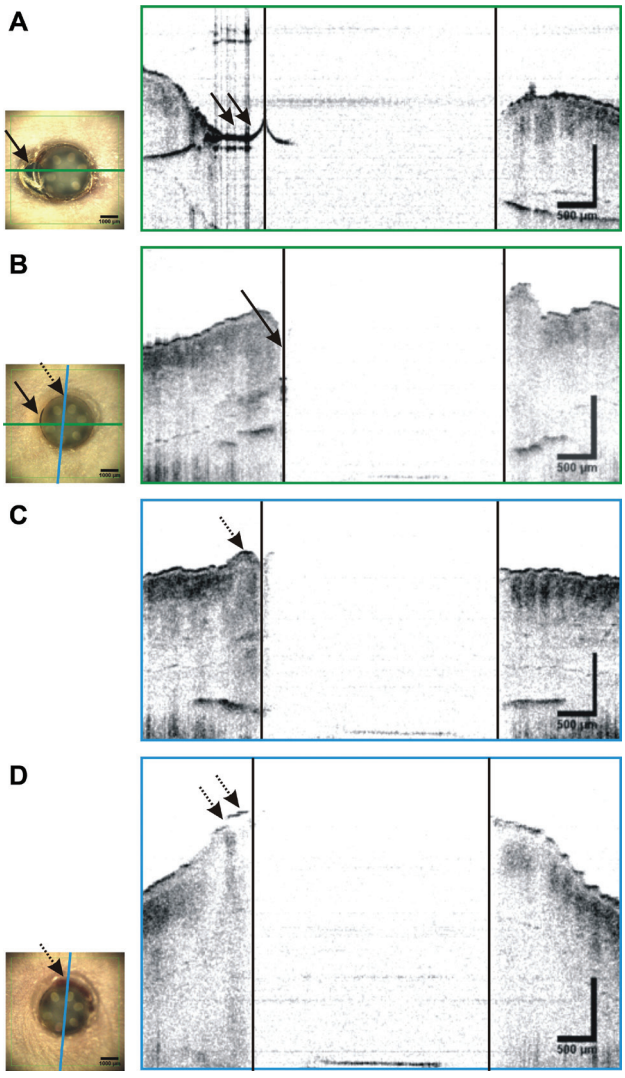

Figure 4 Top-view images (left, scale bar is 1 mm) and OCT B-scans (inverted gray scale: dark color represents high reflectivity; scale bar, 500 µm) at the labeled positions.
Image (A) was acquired *in vivo* on day 7 after implantation and shows the same position like the B-scan in (B) from day 21. The solid-line arrows indicate the gap between implant and skin. Image (C) was taken on day 21 at the later inflammation site and shows early changes of the tissue structure (left part, indicated by dotted-line arrows). Section (D) demonstrates the *post mortem* B-scan of the same region. Inflammation is visible from tissue swelling and progressive tissue structure changes (dotted-line arrows). Axial dimensions are not corrected for the refractive index.

Results

Imaging skin morphology with OCT

An excerpt of a data set from one mouse is presented in Figure 4. The top-view camera images on the left side show the surface of the skin and the pin of the implant in the middle. The green canvas indicates the ROI of the OCT scan. The green and blue lines in the camera images label the position of the presented B-scans. In the OCT scans, the boundaries of the implant pin are shown. The first reflection at the skin surface marks the epidermis. The deeper dark region represents the dermis. The curved black reflection under the skin shows the base of the implant.

The camera image and OCT B-scan presented in Figure 4A were acquired on day 7 after implantation. While the right-hand side shows an example of normal skin morphology at the left-hand side, the hole for the implant was cut too wide, causing a gap between tissue and pin. The implant base was scanned by the OCT

sample beam. The next scan was taken on day 21 after implantation and shows the healing process (Figure 4B). The second B-scan from the data set of day 21 was chosen to show the later inflammation site (Figure 4C, left side of the OCT B-scan). The epidermis was thicker and the structure of the deeper tissue parts was no longer visible. Inflammation was observed on day 52. One OCT scan from the region of inflammation is presented in Figure 4D. The tissue appears much less structured and an overall swelling of the tissue is obvious.

Adapted scanning scheme

The axial motion of the sample caused by breathing and the pulse of the sedated mice generated motion artifacts in the case of *in vivo* scans. This motion is hardly visible in single B-scans as the acquisition time is relatively small, as shown in Figure 5A. The total acquisition time increases for many consecutively taken B-scans and therefore more motion cycles are captured. Shifts and rotations of the surfaces create blurring of the overlay image of five adjacent B-scans from a mode (III) classic 3D data set in Figure 5B. To investigate the implant-tissue interface at several positions around the implant, digital reslicing of the 3D data stack [mode (III) dense scan] at different angles is necessary. A reslice of the *in vivo* 3D data set taken perpendicular to the fast scan axis is shown in Figure 5C. Motion artifacts caused a distortion of the surface contour and a loss of information in the reslices.

Acquisition of B-scans using a spoke pattern [mode (II) scanning scheme] generates 2D optical sections with significantly reduced motion artifacts at arbitrary angular positions, as shown in an example B-scan in Figure 5D.

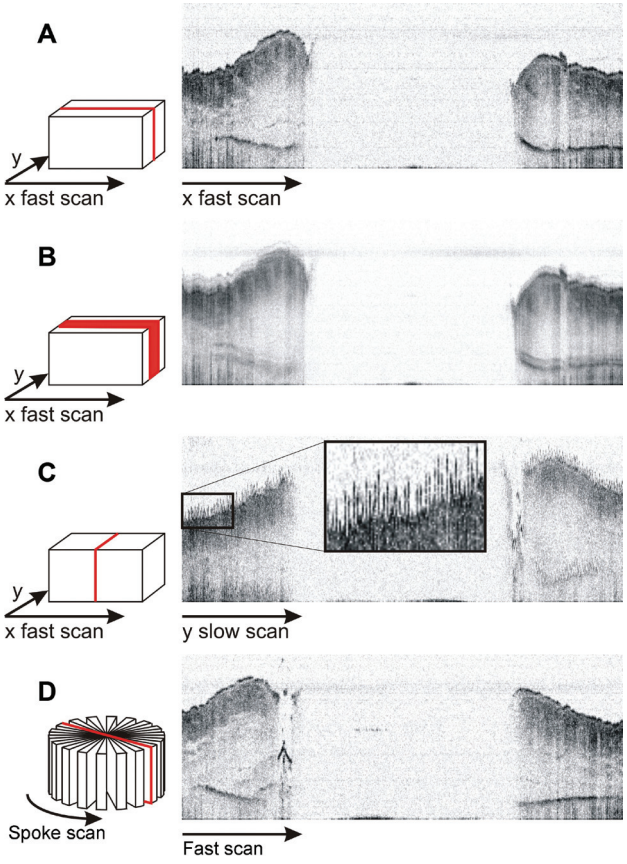

Figure 5 OCT images with inverted gray scale; dark color represents high reflectivity.
Scale: the pin of the implant in the middle of the image (lack of image information) is 3-mm wide. Three-dimensional data sets were acquired by scanning the area sequentially. (A) Single OCT B-scan and (B) overlay of five adjacent B-scans from an *in vivo* 3D scan. (C) Reslice of an *in vivo* 3D data set sliced perpendicular to the fast scan axis. Artifacts are due to sample movements. (D) In spoke pattern scans, the fast scanning axis is rotated.

Image processing

Figure 6 shows the results of image processing of the original B-scans (A) without (B) and after motion compensation (C). In the original images, the implant base appears as a curved line because of the refraction of the sample beam at the tissue surface and the refractive index of the tissue. The image undistortion algorithm searches for the highest support of a base plane with the implant base reflex within the full 3D data set. The comparative images in Figure 6B and C illustrate the need for motion correction before image undistortion. As without motion compensation, most of the true implant baseline was missed because the motion shift occurring throughout several B-scans was not taken into account. The algorithm calculated an overall refractive index of 1.39. For each A-scan image, data beneath the upper surface of the skin were tilted towards the local surface normal and the axial length was scaled by the refractive index. In the processed B-scan, the implant base appears now as a straight line (Figure 6C). Its geometrical height can be measured in further image processing steps.

Quantitative analysis of OCT B-scans at the implant-tissue interface

For quantitative analysis, three morphological parameters were assessed by the image processing algorithm. The distance to the pin was the gap between the implant-tissue interface and the highest point of the skin surface.

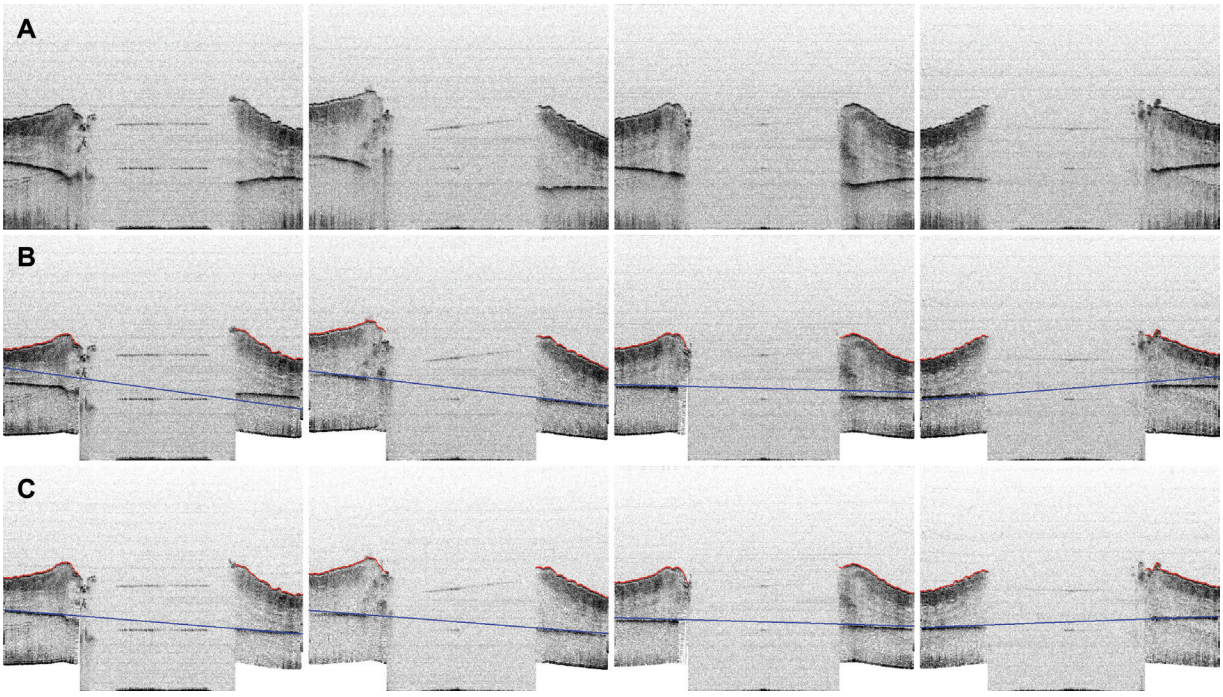

Figure 6 The result of image processing is shown on a sequence of spoke pattern B-scans.
(A) Unprocessed images; (B) image processing without motion compensation; and (C) image processing after motion compensation. In the original B-scans (A), the base of the implant appears as a curved line. In images (B) and (C), the red line marks the segmented surface contour and the blue line refers to the estimated position of the base line. In image (C), these lines show better accordance with the base line reflexes than in the images without motion compensation (B). n=1.43.

Downgrowth was defined as the distance from that point to the outer rim of the pin. Tissue thickness was measured from the highest point of the skin surface down to the base of the implant. Analyzing a spoke pattern data set with 72 B-scans, the parameters were measured for 144 positions around at the implant-tissue interface. As labeled in Figure 7A, 0° is the position at the left side of the pin and 180° defines the opposite side, being represented in the same B-scan. In Figure 7C, the morphometric parameters for one mouse at day 26 after implantation are displayed graphically. The distance to the pin and epithelial downgrowth significantly increased in a small area localized at the inflammation site. The tissue thickness is found to be increased for a larger area covering half of the implant-tissue interface. The B-scan in Figure 7B reveals a position of raised tissue thickness, the distance to the pin, and downgrowth at the right side.

Discussion

OCT was used for *in vivo* monitoring of implant-tissue interfaces. This non-contact optical technique enabled observation of the morphological changes due to, e.g., inflammation, without impairing the biological mechanisms. Repetitive measurements on the same animal were possible and allowed for the monitoring of the ongoing immune reaction, as the animals did not need to be killed like in previously published work [6].

Having a resolution of approximately 10 µm, OCT does not reach cellular resolution but is still able to visualize skin layers. Its resolution fills the gap between histology and clinical imaging modalities such as sonography or X-ray and therefore is more capable for *in vivo* investigation of percutaneous devices than, e.g., the X-ray photographs used by Shin and Akao [20].

The general problem of motion artifacts is partly solved by implementing a scanning scheme that uses the fast scanning axis for rapid acquisition of cross-sectional images of the desired planes around the metal implant. Residual axial sample movement within the acquisition time of one B-scan did not hinder qualitative analysis and morphology visualization as all tissue layers are equally deformed. Motion during the acquisition time of one A-line caused reduced signal-to-noise ratio owing to the fringe washout of the interference signal during the integration time of the global shutter line detector, as described by Yun et al. [29] as well as by Walther et al. [25], and might have caused the poor image quality of

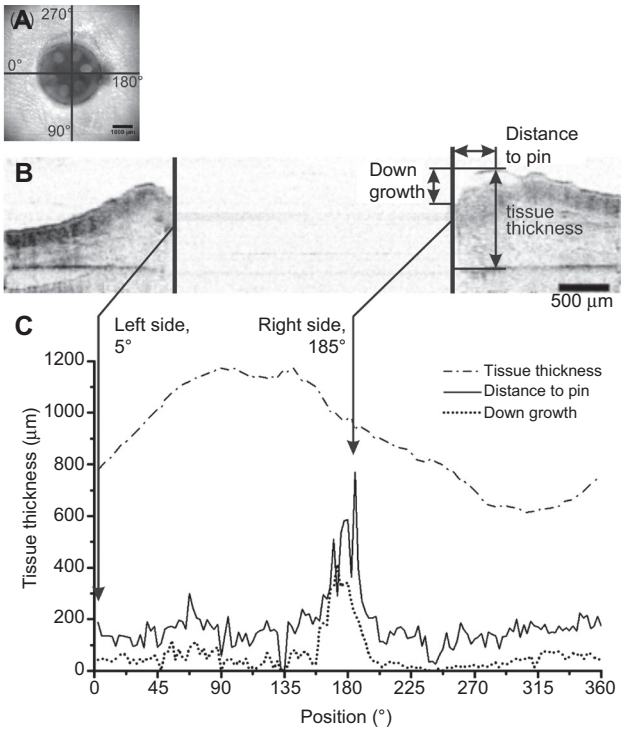

Figure 7 Camera image (A), B-scan (B), and morphometric parameters (C) for one mouse. Position markers in the camera image reveal the angular positions of the morphological parameters. In the B-scan (at position 5° left side and 185° right side), the morphometric parameters are drawn in schematically. The graph shows the measured parameters of downgrowth, distance to the pin, and tissue thickness. The arrows indicate the corresponding values for the B-scan above.

some B-scans. However, apart from qualitative analysis, a quantitative analysis is desirable to gain objective data and analyze large data sets. Before quantitative analysis, we addressed the problem of image distortion due to ray refraction in the sample.

The ability of OCT to measure optical path differences was first used to measure refractive index of excised skin by Tearney et al. [22] and applied to isolated crystalline lenses by different groups [10, 23, 27]. In our study, the reference plane for geometrical distances was formed by the implant base and therefore refractive index estimation for tissue *in situ* without preparation was possible.

As refraction on the sample surface is a 3D problem, the analysis of whole 3D stacks was necessary. As sample motion caused untrue sample tilt in single B-scans and relative movement within B-scans, the data set needed to be motion compensated to apply the image undistortion algorithm on *in vivo* data. Qualitatively, the OCT scans showed surprisingly high intra-individual differences of morphology of the skin next to the implant. A clear relation between morphological features and susceptibility to inflammation was impaired by this heterogeneity. Having analyzed the full 3D image data instead of only three arbitrary micron sections per implant, as published by Pendegrass et al. [19], we suggest to perform further studies on the findings about the significant correlations between morphometric parameters and sensitivity to inflammation.

The hypothesis that the index of refraction might be an early indicator of inflammation could not be answered, as the estimated overall refractive indices showed no consistent result. Whether better results can be obtained by segmentation of single tissue layers, as presented by Hori et al. [7], and allocation of different refractive indices may be addressed in future studies.

Acknowledgments: This work is supported in part by funding from the German Research Foundation (DFG) and the Collaborative Research Center, Transregio 37. Some authors acknowledge the financial support of the BMBF project TExoPro and the NSF-ERC for Revolutionizing Metallic Biomaterials.

Received July 24, 2012; accepted April 12, 2013; online first May 17, 2013

References

[1] Ballard DH. Generalizing the Hough transform to detect arbitrary shapes. Pattern Recognit 1981; 13: 111–122.
[2] Cleveland WS. Robust locally weighted regression and smoothing scatterplots. J Am Stat Assoc 1979; 74: 829–836.
[3] Fercher F, Hitzenberger K, Kamp G, El-Zaiat SY. Measurement of intraocular distances by backscattering spectral interferometry. Optics Commun 1995; 117: 43–48.
[4] Gambichler T, Jaedicke V, Terras S. Optical coherence tomography in dermatology: technical and clinical aspects. Arch Dermatol Res 2011; 303: 457–473. DOI:10.1007/s00403-011-1152-x.
[5] Gladkova ND, Petrova GA, Nikulin NK, et al. *In vivo* optical coherence tomography imaging of human skin: norm and pathology. Skin Res Technol 2000; 6: 6–16.
[6] Heaney TG, Doherty PJ, Williams DF. Marsupialization of percutaneous implants in presence of deep connective tissue. J Biomed Mater Res 1996; 32: 593–601. DOI:gt;3.0.CO;2-F.
[7] Hori Y, Yasuno Y, Sakai S, et al. Automatic characterization and segmentation of human skin using three-dimensional optical coherence tomography. Opt Express 2006; 14: 1862–1877.
[8] Huang D, Swanson EA, Lin CP, et al. Optical coherence tomography. Science 1991; 254: 1178–1181.

[9] Kang W, Wang H, Wang Z, et al. Motion artifacts associated with *in vivo* endoscopic OCT images of the esophagus. Optics Express 2011; 19: 898–905.
[10] Kim E, Ehrmann K, Uhlhorn S, Borja D, Parel J-M. Automated analysis of OCT images of the crystalline lens. In: Manns F, Soderberg PG, Ho A, editors. Proc SPIE 7163, Ophthalmic technologies XIX 2009: 716313. DOI:10.1117/12.809986.
[11] Klein T, Wieser W, Eigenwillig CM, Biedermann BR, Huber R. Megahertz OCT for ultrawide-field retinal imaging with a 1050 nm Fourier domain mode-locked laser. Optics Express 2011; 19: 3044–3062.
[12] Li SZ. Markov random field modeling in image analysis, 3rd ed. London: Springer Publishing Company 2009.
[13] Liew YM, McLaughlin RA, Wood FM, Sampson DD. Motion correction of *in vivo* three-dimensional optical coherence tomography of human skin using a fiducial marker. Biomed Optics Express 2012; 3: 1774–1786. DOI:10.1364/BOE.3.001774.
[14] Liew YM, McLaughlin RA, Wood FM, Sampson DD. Reduction of image artifacts in three-dimensional optical coherence tomography of skin *in vivo*. J Biomed Optics 2011; 16: 116018. DOI:10.1117/1.3652710.
[15] McLaughlin RA, Armstrong JJ, Becker S, et al. Respiratory gating of anatomical optical coherence tomography images of the human airway. Optics Express 2009; 17: 6568–6577.
[16] McNabb RP, Larocca F, Farsiu S, Kuo AN, Izatt JA. Distributed scanning volumetric SDOCT for motion corrected corneal biometry. Biomed Optics Express 2012; 3: 2050–2065. DOI:10.1364/BOE.3.002050.
[17] Müller O, Donner S, Klinder T. Compensating motion artifacts of 3D *in vivo* SD-OCT scans. Med Image Comput Comput Assist Interv 2012; 7510: 198–205. DOI:10.1007/978-3-642-33415-3_25.
[18] Müller O, Donner S, Klinder T, et al. Model based 3D segmentation and OCT image undistortion of percutaneous implants. In: 14th International conference on medical image computing and computer assisted intervention (MICCAI) 2011. Lecture notes in computer science, vol. 6893. Berlin: Springer 2011: 454–462.
[19] Pendegrass CJ, Goodship AE, Blunn GW. Development of a soft tissue seal around bone-anchored transcutaneous amputation prostheses. Biomaterials 2006; 27: 4183–4191. DOI:10.1016/j.biomaterials.2006.03.041.
[20] Shin Y, Akao M. Tissue reactions to various percutaneous materials with different surface properties and structures. Artif Organs 1997; 21: 995–1001.
[21] Staubach K-H, Grundei H. The first osseointegrated percutaneous anchor for an exoprosthesis, for routine use in above-knee amputees. Biomed Technik 2001; 46: 355–361.
[22] Tearney GJ, Brezinski ME, Southern JF, Bouma BE, Hee MR, Fujimoto JG. Determination of the refractive index of highly scattering human tissue by optical coherence tomography. Opt Lett 1995; 20: 2258–2260.
[23] Uhlhorn SR, Borja D, Manns F, Parel J-M. Refractive index measurement of the isolated crystalline lens using optical coherence tomography. Vision Res 2008; 48: 2732–2738. DOI:10.1016/j.visres.2008.09.010.
[24] von Recum AF. Applications and failure modes of percutaneous devices: a review. J Biomed Mater Res 1984; 18: 323–336. DOI:10.1002/jbm.820180403.
[25] Walther J, Krüger A, Cuevas M, Koch E. Effects of axial, transverse, and oblique sample motion in FD OCT in systems with global or rolling shutter line detector. J Opt Soc Am A Optics Image Sci Vis 2008; 25: 2791–2802.
[26] Weissman J, Hancewicz T, Kaplan P. Optical coherence tomography of skin for measurement of epidermal thickness by shapelet-based image analysis. Opt Express 2004; 12: 5760–5769.
[27] Westphal V, Rollins A, Radhakrishnan S, Izatt J. Correction of geometric and refractive image distortions in optical coherence tomography applying Fermat's principle. Opt Express 2002; 10: 397–404.
[28] Xie Y. A new efficient ellipse detection method. In: Kasturi R, Laurendeau D, Suen C, editors. International conference on pattern recognition 2002: 0–3.
[29] Yun SH, Tearney GJ, De Boer JF, Bouma BE. Motion artifacts in optical coherence tomography with frequency-domain ranging. Opt Express 2004; 12: 2977–2998.